

A Study of Deformation and Fracture of the Eutectic in an Additively Manufactured Al-Si Composite Alloy

A. V. Zemlyanov¹, D. D. Gatiyatullina^{1,2}, V. R. Utyaganova¹, E. Dymnich¹, N. N. Shamarin¹,
S. Yu. Nikonov¹, V. A. Romanova¹, A. S. Kulkov¹, and R. R. Balokhonov^{1*}

¹ Institute of Strength Physics and Materials Science, Siberian Branch, Russian Academy of Sciences,
Tomsk, 634055 Russia

² National Research Tomsk State University, Tomsk, 634050 Russia

* e-mail: rusy@ispms.ru

Received June 8, 2023; revised July 10, 2023; accepted July 26, 2023

Abstract—Experimental and numerical studies were conducted on AlSi12 alloy fabricated by wire-feed electron beam additive manufacturing to examine the structure, thermomechanical behavior and fracture of a eutectic microvolume at the scale of several microns. Dynamic boundary value problems were solved under plane strain conditions. The composite structure of the eutectic phase consisting of an aluminum matrix and silicon particles was taken into account explicitly in the calculations. Isotropic models of the thermoelasto-plastic matrix and elastic-brittle particles were implemented in ABAQUS/Explicit. Composite deformation was calculated both with and without allowance for residual stresses caused by cooling of the composite after its fabrication. It was shown that after the cooling of the eutectic, silicon particles are compressed, and the aluminum matrix is under both bulk compressive and tensile as well as under pure shear stresses. It was found that residual stresses play a negative role at the stages of intense deformation of the composite. The fracture strain of the eutectic strongly depends on the yield point of the matrix, while the ultimate fracture stress varies but only slightly. Favorable morphology of silicon particles was determined which prevents early fracture of the eutectic.

Keywords: electron beam additive manufacturing, AlSi12 alloy, numerical simulation, residual stresses, plastic strain localization, fracture

DOI: 10.1134/S1029959923060073

1. INTRODUCTION

Aluminum alloys combine low density and relatively high strength, which make them attractive for various industrial applications. Aluminum-silicon alloys AlSi12, also called silumins, are promising materials for the manufacture of components and structures due to low thermal expansion, good corrosion resistance and wear resistance [1–3]. Conventionally, AlSi12 alloys are characterized by good castability and machinability. The eutectic of an aluminum-silicon alloy consists of a hard brittle Si phase in a softer matrix of pure Al. That is why most of the mechanical properties of the material, especially elongation to failure, are determined by the eutectic microstructure. One of the ways to improve the mechanical properties of Al-Si cast alloys is their modification by the addition of alloying elements to the aluminum melt in order to form a fine fibrous eutectic silicon struc-

ture during solidification. The Al-Si eutectic can be modified either by the addition of certain elements (chemical modification) or by high cooling rates (quench modification) [4]. The refinement of the Si phase, including by adding strontium or sodium to the Al-Si melt before casting, has been studied in detail by many authors [5, 6]. A low cooling rate during casting promotes the nucleation of needle-like or coarse eutectic Si, which greatly reduces the mechanical properties of the alloy and its service life in aggressive environments [7]. Thus, modified and refined eutectic (α +Si) phases improve the mechanical properties of aluminum-silicon alloys and expand their application range. This alloy is most commonly used in the production of pistons and engine blocks.

The growing needs of the automotive and aerospace industries for highly loaded complex-shape parts and components have led to great advances in

additive manufacturing. These technologies have obvious advantages over conventional methods, including virtually waste-free production and resulting products without welds and other joints. Rapid solidification and high cooling rates lead to the formation of a finer microstructure compared to casting [8, 9]. The most common additive manufacturing technology for the production of aluminum-silicon alloys is selective laser melting [10, 11]. The use of a pulsed laser instead of a continuous-wave source allowed greater control over heat input and silicon grain refinement to less than 200 nm [10]. The effect of specific laser energy on microstructure evolution in an additively manufactured alloy was studied in [11]. The mechanical properties of AlSi12 produced by selective laser melting are not inferior to those of the cast alloy [12]. In [13], AlSi12 alloy samples were tested at high temperatures. The results showed that AlSi12 alloy fabricated by selective laser melting is well suited for the automotive industry to produce pistons and cylinder heads. The use of wire feedstock for laser melting

saves more than 80% of energy compared to other laser technologies [14]. Laser beam deposition of Al 5087 alloy wire was investigated in [15] by producing single tracks and multi-track walls to select optimal conditions for stable deposition. Most of the resulting samples were characterized by low porosity. Among the existing 3D printing technologies, electron beam additive manufacturing (EBAM) shows much promise for producing high-quality products with low-defect structure. It provides easier control over the composition of a complex-shape part due to the possibility to adjust the printing process parameters, such as wire feeding speed and heat input [16].

The eutectic of the AlSi12 alloy considered in this work is a composite material consisting of an aluminum matrix with silicon particles. Earlier we investigated some aspects of the deformation and fracture of particle-reinforced metal matrix composites [17–19]. We studied the effect of the volume fraction and spatial distribution of reinforcement particles, strength and ductility of the matrix and particle materials on

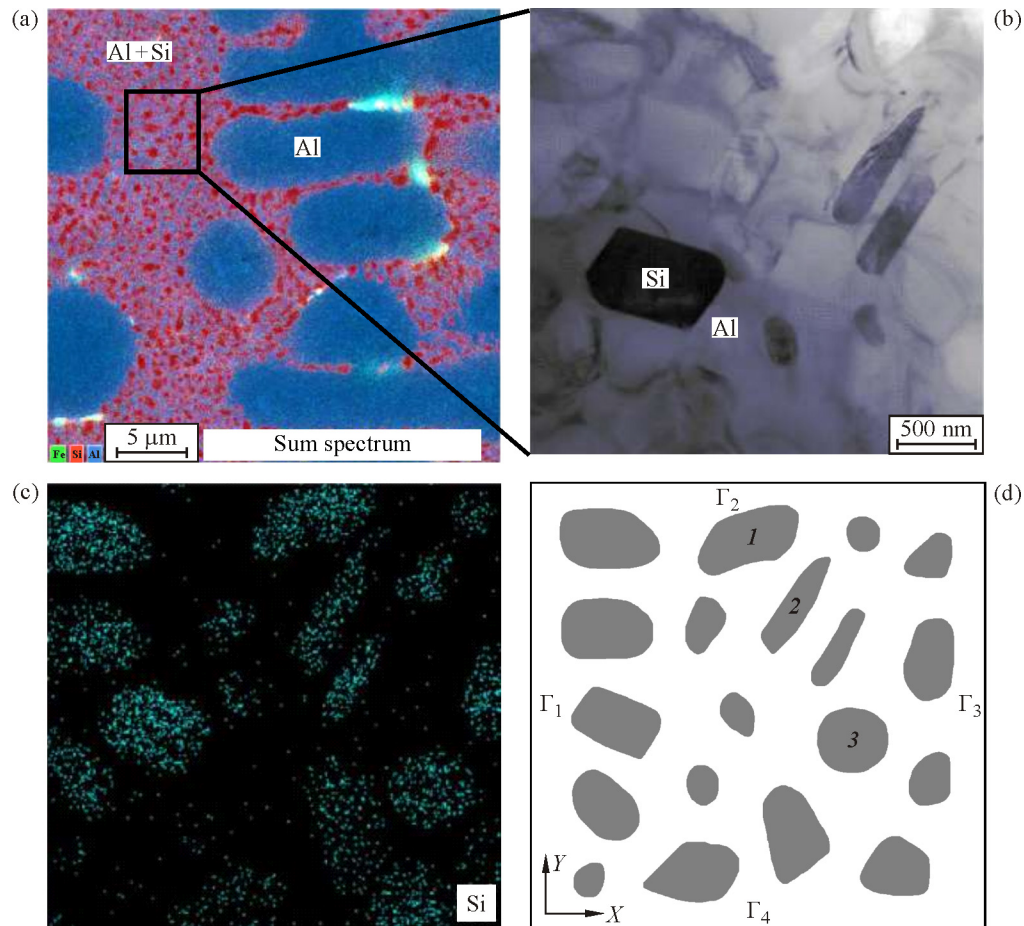


Fig. 1. Dendritic structure and eutectic network (a), fragment of the eutectic (b), elemental analysis (c), and model structure of printed AlSi12 alloy (d) (color online).

the macroscopic response of the composite. Special attention was paid to residual stresses that arise in the composites during manufacture and affect the mechanical behavior of the material in a future service environment [20].

This work investigates the thermomechanical behavior of a representative microvolume of the eutectic formed in AlSi12 alloy produced by wire-feed electron beam additive manufacturing.

2. PROBLEM FORMULATION

The structure of AlSi12 alloy was studied experimentally. EBAM samples were printed using selected electron beam melting parameters and ESAB OK Autrod 4047 wire (1.2 mm). The setup for wire-feed electron beam additive manufacturing was designed and constructed at the Institute of Strength Physics and Materials Science SB RAS (Tomsk, Russia). The following printing parameters were used: chamber pressure $\sim 5 \times 10^{-5}$ Pa, accelerating voltage 30 kV, table travel speed 540 mm/min, beam sweep diameter ~ 4 mm, circular sweep mode. The total number of deposited layers was 40. The beam current decreased exponentially from 38 (layer 1) to 24 mA (layers 15–40). Sections for SEM and TEM microstructural studies were cut from the middle of the samples. The experimental results are presented in Fig. 1. The image in Fig. 1a was obtained on a Tescan Mira 3 LMU SEM microscope with an EDS detector.

TEM foils were prepared by mechanical grinding of plates to 150 μm thickness followed by ion milling at 6 kV for 12 hours. The images in Figs. 1b and 1c were obtained on a JEM-2100 TEM microscope with an EDS detector. Energy dispersive X-ray analysis revealed the formation of a dendritic structure during melt crystallization: there are individual aluminum dendrites of the order of tens of micrometers surrounded by the eutectic network (Fig. 1a). On a lower scale of the order of a few micrometers, submicron silicon particles in the aluminum matrix are clearly visible in the eutectic (Figs. 1b and 1c).

By graphically processing (binarizing) the experimental image of a eutectic microvolume, we obtained a model composite structure with the spatial domain dimensions of the order of $2.5 \times 2.5 \mu\text{m}$ (Fig. 1d), which was discretized by a regular rectilinear mesh with 480×480 square finite elements. Two-dimensional dynamic boundary value problems of loading the composite were solved for plane stress in ABAQUS/Explicit. The significant difference in the thermal expansion coefficients of silicon and alu-

minum can cause high residual stresses in the eutectic during cooling of the dendritic structure. The influence of residual stresses on the behavior of the composite was studied through calculations of the thermomechanical loading of the eutectic. The thermoelastoplastic behavior of the matrix was described using the Duhamel–Neumann relations:

$$\begin{aligned} \dot{\sigma}_{ij} &= -\dot{P}\delta_{ij} + \dot{S}_{ij} \\ &= K(\dot{\varepsilon}_{kk} - 3\alpha\dot{T})\delta_{ij} + 2\mu(\dot{\varepsilon}_{ij} - \dot{\varepsilon}_{kk}\delta_{ij}/3 - \dot{\varepsilon}_{ij}^p), \end{aligned} \quad (1)$$

where σ_{ij} and S_{ij} are the stress tensor and deviatoric stress tensor components, P is the pressure, ε_{ij} and ε_{ij}^p are the components of the total strain tensor and plastic strain tensor, δ_{ij} is the Kronecker delta, K and μ are the bulk compression and shear moduli, α is the coefficient of thermal expansion, T is temperature, and the dot means the time derivative.

The plastic flow rule $\dot{\varepsilon}_{ij}^p = \lambda \dot{S}_{ij}$ associated with the yield criterion $\sigma_{\text{eq}} - Y_0(\varepsilon_{\text{eq}}^p) = 0$ is used. Here λ is a scalar factor that is identically equal to zero in the elastic region. The matrix is assumed to strain-harden; the isotropic hardening function has the form

$$Y_0(\varepsilon_{\text{eq}}^p) = \sigma_s - (\sigma_s - \sigma_0)\exp(-\varepsilon_{\text{eq}}^p/\varepsilon_r^p), \quad (2)$$

where σ_s and σ_0 are the ultimate strength and yield point, and ε_r^p is the strain hardening parameter. In the general case, expressions for the equivalent stress and accumulated equivalent plastic strain read

$$\begin{aligned} \sigma_{\text{eq}} &= \frac{1}{\sqrt{2}} [(\sigma_{11} - \sigma_{22})^2 + (\sigma_{22} - \sigma_{33})^2 \\ &+ (\sigma_{33} - \sigma_{11})^2 + 6(\sigma_{12}^2 + \sigma_{23}^2 + \sigma_{31}^2)]^{1/2}, \end{aligned} \quad (3)$$

$$\begin{aligned} \varepsilon_{\text{eq}}^p &= \frac{\sqrt{2}}{3} [(\varepsilon_{xx}^p - \varepsilon_{yy}^p)^2 + (\varepsilon_{zz}^p - \varepsilon_{yy}^p)^2 \\ &+ (\varepsilon_{xx}^p - \varepsilon_{zz}^p)^2 + 6(\varepsilon_{xy}^p + \varepsilon_{yz}^p + \varepsilon_{xz}^p)]^{1/2}. \end{aligned} \quad (4)$$

The thermoelastic response of silicon particles is described by Eq. (1), where $\dot{\varepsilon}_{ij}^p = 0$. Fracture of aluminum is assumed to occur upon reaching a critical value of the accumulated equivalent plastic strain

$$\varepsilon_{\text{eq}}^p = \varepsilon_{\text{fr}}^p. \quad (5)$$

Silicon is assumed to be elastic-brittle. Fracture of particles is taken into account using a Huber criterion of maximum equivalent stress that accounts for the type of stress:

$$\sigma_{\text{eq}} = C_{\text{ten}}, \text{ if } \varepsilon_{kk} > 0. \quad (6)$$

Criteria (5) and (6) operate on the following principle. If the accumulated equivalent plastic strain in any region of the matrix exceeds $\varepsilon_{\text{fr}}^p$, or when the equivalent stress in a local region of a particle subjected to bulk tension exceeds the silicon tensile

Table 1. Physical and mechanical properties of aluminum and silicon

Material	ρ , g/cm ³	K , GPa	μ , GPa	σ_s , MPa	σ_0 , MPa	ε_r^p , %	ε_{fr}^p , %	C_{ten} , MPa	α , 10 ⁻⁶ °C ⁻¹
Matrix									
Al30	2.7	66	26	82	30	10	35	–	22
Al45				97	45				
Al60				112	60				
Particles									
Si	2.33	98	60	–	–	–	–	172	2.5

strength C_{ten} , this region is considered failed. Then, if this region is under bulk tension, the stress tensor components in it become equal to zero: $\sigma_{ij}=0$, while if the region is under bulk compression, only the deviatoric stress tensor components are zero: $S_{ij}=0$. Thus, the failed region does not resist shear and bulk tension, but continues to resist bulk compression.

Equations (1)–(6) were implemented in ABAQUS/Explicit through a VUMAT subroutine written in Fortran.

The mechanical properties of aluminum and silicon are well known and can be easily found in the literature, e.g., in [21]. The plasticity characteristics of pure aluminum can vary depending on the defect structure formed by different manufacturing and processing techniques [22]. Due to rapid solidification in additive manufacturing, aluminum formed in the eutectic network between silicon nanoparticles may have a nanodefekt structure. The plastic properties of such a material are unknown and may vary depending on melting and heat treatment conditions; their determination requires separate experimental and numerical studies, which are beyond the scope of the present paper. However, it seems appropriate to study how the strength, deformation and fracture behavior of the composite depend on the mechanical properties of the matrix material. Therefore, in this study, the yield point of aluminum was varied within the model range from 30 to 60 MPa. In order to evaluate the influence of this parameter on the strength of the composite, other conditions such as strain hardening behavior and the ultimate fracture strain of aluminum were assumed to remain unchanged. The corresponding matrix materials are arbitrarily called Al30, Al45, and Al60 (Table 1). The characteristics and experimental constants used in the calculations are given in Table 1.

Calculations were carried out for two types of loading applied to composites. The first type of problems (without taking into account cooling-induced

residual stresses (NRS)) describes the stretching of the material along the X or Y axis (Fig. 1d) from the initial unstrained state:

$$u_i(x, y) = 0, \sigma_{ij}(x, y) = 0, \rho(x, y) = \rho_0(x, y). \quad (7)$$

The second type of problems (with taking into account cooling-induced residual stresses (RS)) describes a combined thermomechanical loading, in which the eutectic is cooled in the first step from state (7) from 350°C to room temperature 23°C. The temperature decreases linearly, while on all faces of the computational domain ($\Gamma_{i=1,\dots,4}$ in Fig. 1d) free surface conditions are satisfied:

$$\sigma_{ij}(x, y, t)n_j = 0. \quad (8)$$

As a result of cooling, residual stresses arise in the material due to the difference in the thermoelastic properties of the particles and the matrix. In the second step, the cooled material is subjected to tension.

Uniaxial tension of the material in both cases (NRS and RS) is modeled by the boundary conditions: $u_x(x, y, t) = -V$ and $u_x(x, y, t) = V$ on the left Γ_1 and right Γ_3 boundaries of the computational domain under tension along X , $u_y(x, y, t) = -V$ and $u_y(x, y, t) = V$ on the upper Γ_2 and lower Γ_4 boundaries of the computational domain under tension along Y , and $\sigma_{xy}(x, y, t) = 0$. On the remaining domain boundaries, i.e., on Γ_2 and Γ_4 under tension along X and on Γ_1 and Γ_3 under tension along Y , free surface conditions (8) are specified. The mass velocity V is equal to 5×10^{-5} cm/ μ s. Although we use a dynamic formulation of the problem, the constitutive equations take no account of the material sensitivity to strain rate and temperature changes. When simulating quasi-static tension, the mass velocity was gradually increased. The temperature was also changed slowly enough to minimize the dynamic effects associated with the generation and propagation of elastic waves at the matrix–particle interface due to different elastic moduli and thermal expansion coefficients of silicon and aluminum.

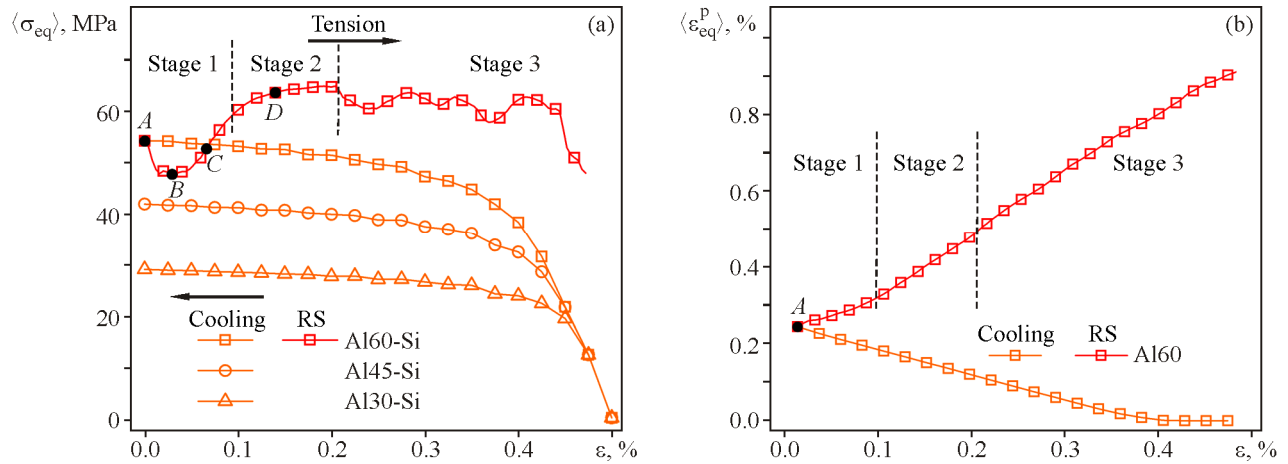


Fig. 2. Characteristic stages of deformation and fracture of the eutectic. Averaged flow curves during cooling of composites with different matrix yield points, cooling and subsequent stretching (a) and the accumulated equivalent plastic strains in the Al60 matrix (b) (color online).

3. SIMULATION RESULTS

3.1. Thermomechanical Deformation of the Eutectic

Let us consider the general deformation behavior of the composite structure of the eutectic phase under mechanical loading after precooling (RS) for an aluminum matrix with a yield point of 60 MPa. Figure 2a shows macroscopic flow curves during cooling (orange curve with square symbols) and subsequent stretching along Y (red curve with square symbols). Hereinafter the value of the equivalent stress averaged over the computational domain (3) is plotted along the ordinate axis:

$$\langle \sigma_{eq} \rangle = \frac{\sum_{k=1,N} \sigma_{eq}^k S^k}{\sum_{k=1,N} S^k},$$

where N is the number of cells in the computational mesh, and S^k is the local volume of the k th cell. The strain plotted along the abscissa axis is the relative elongation of the computational domain in the X or Y direction (Fig. 1d): $\epsilon = (L - L_0)/L_0$, where L_0 and L are the initial and current length of the model sample. The tensile flow curves for the RS case start at 0% strain for ease of comparison with the curves for the NRS case. In fact, the residual strain along X averaged over all lines $Y = \text{const}$ after cooling the composite is about -0.5% . Therefore, the graphs in the RS case are shifted to the right by 0.5% .

It was found that cooling-induced residual stresses negatively affect the strength of the eutectic, leading to premature fracture of particles. This corresponds to a drop in the current flow stress in the initial por-

tion of the flow curve with further stretching. Initially, the flow curve is linear during cooling due to elastic compression of the matrix at the beginning of cooling (Fig. 2a), caused by the absence of plastic strains in the range $\epsilon = 0.5 - 0.45\%$ (Fig. 2b). After reaching the yield point of 60 MPa, nonuniform plastic flow begins in the matrix, and the flow curve shows a nonlinear strain dependence of stresses (Fig. 2a) and accumulated equivalent plastic strains $\langle \epsilon_{eq}^p \rangle$ averaged over the computational domain of the matrix (Fig. 2b). The stress and strain fields in the particles and the matrix after cooling are shown in Fig. 3 (state A). Aluminum, which has a greater thermal expansion coefficient than silicon particles, exerts all-round compression on the particles. Therefore, the particles after cooling experience only bulk compression (blue color on the pressure scale). Bulk residual tensile and compressive stresses arise in the matrix (red and blue colors on the pressure scale). Compressive stresses are concentrated around the particles at the interface convexities, while at a distance from the particles there are circular bulk tensile regions with maximum negative pressures near free surfaces and between closely spaced particles (Fig. 3, P distributions for state A).

All-round compression of the eutectic during cooling causes the concentration of equivalent stresses in silicon particles near the curvilinear parts of the interface and the formation of circular regions with higher equivalent stresses around the particles in the aluminum matrix (cf. P and ϵ_{eq}^p distributions for state A in Fig. 3). Noteworthy is that the regions with high values of σ_{eq} show areas where the pressure is

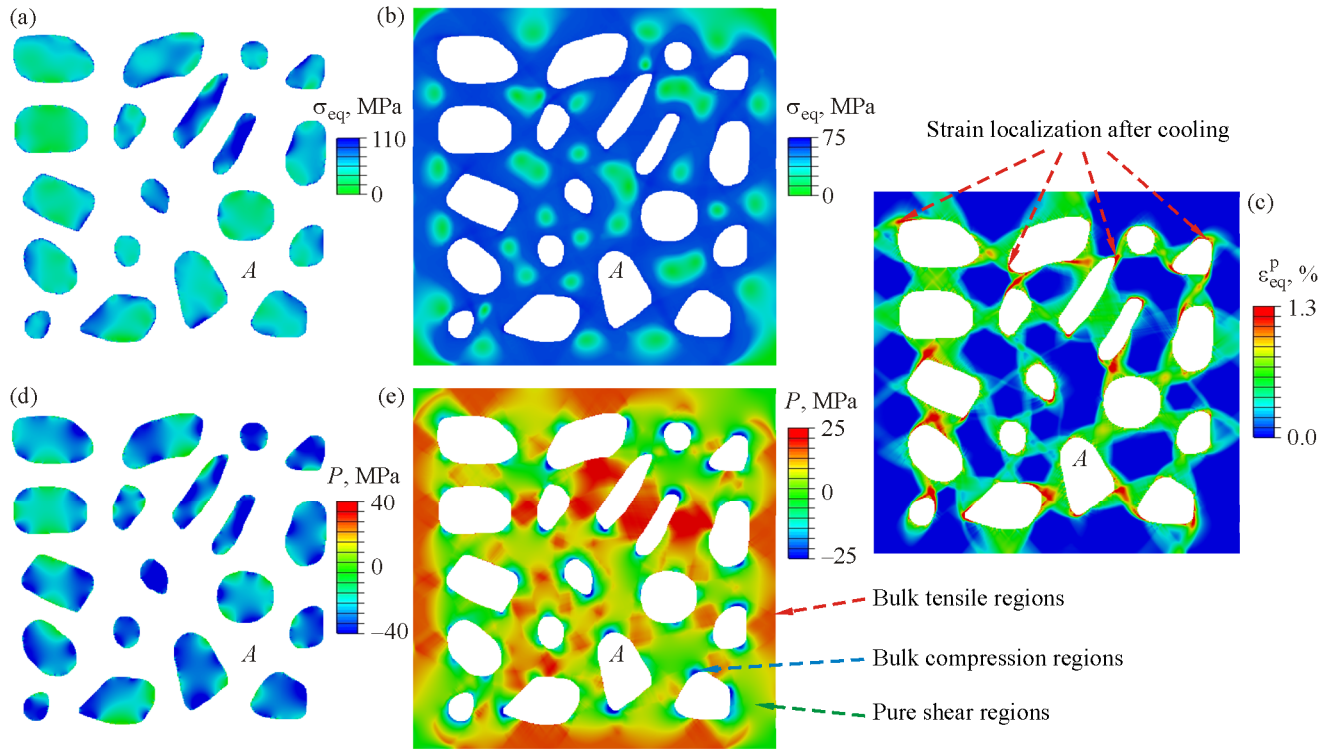


Fig. 3. Stress-strain state in Si particles (a, d) and Al60 matrix (b, c, e) after cooling. State *A* (color online).

zero (green color for P distributions for state *A*). This means that these areas are under pure shear.

Plastic flow is localized around particles in the matrix, and the maximum plastic strains are observed mainly in the regions of bulk compression and shear (cf. P and ϵ_{eq}^p distributions for state *A* in Fig. 3). The described stress-strain state, which results from cooling of the composite, completely determines the deformation stages of the composite during subsequent uniaxial tension (Fig. 2). It was found that plastic flow localization and stress concentration at each stage of deformation develop consistently in relation to each other.

At stage 1, the stress-strain state gradually changes from multiaxial to uniaxial one. Immediately after cooling, at the start of tensile loading, the stresses on the flow curve drop. After reaching a minimum value, they begin to increase. The stress drop is due to the fact that the particles are in a compressed state after cooling. When the composite is stretched, the particles also stretch, the compressive stresses decrease (cf. particle pressure for states *A* and *B* in Figs. 3 and 4) and become zero. Next, tensile stresses appear (states *C* and *D* in Fig. 4) with maximum values at the convex regions of the particles.

Analysis of stresses separately in the particles and the matrix revealed that the average stresses in the matrix also decrease (Fig. 5a). This happens, firstly, because the stress drop in the particles contributes to unloading of the matrix. Secondly, a small number of local compressed regions of the matrix are unloaded independently: blue areas of the P distribution for state *A* in Fig. 3 reduce in size (state *B*) and finally disappear (states *C* and *D*) in Fig. 4. As a consequence, the accumulation of plastic strains in these regions stops at stage 1 and then starts again at stage 2 when they begin to stretch and the equivalent stresses in them exceed the yield point. This leads to slower plastic strain accumulation in the matrix at stage 1 than at stage 2 (Fig. 2b). Thus, the cooling-induced compressive residual stresses both in the particle and in the matrix play a positive role, delaying the formation of local tensile regions at the early stages of subsequent stretching of the composite.

The particle pressure drops sharply with the application of tension and continues to rapidly decrease, slower or faster, at stage 1 in which the multiaxial stress-strain state changes to uniaxial one. At stage 2 with fully-developed plastic flow in aluminum, the drop in average particle pressure gradually slows down (Fig. 5b). The average pressure level in the ma-

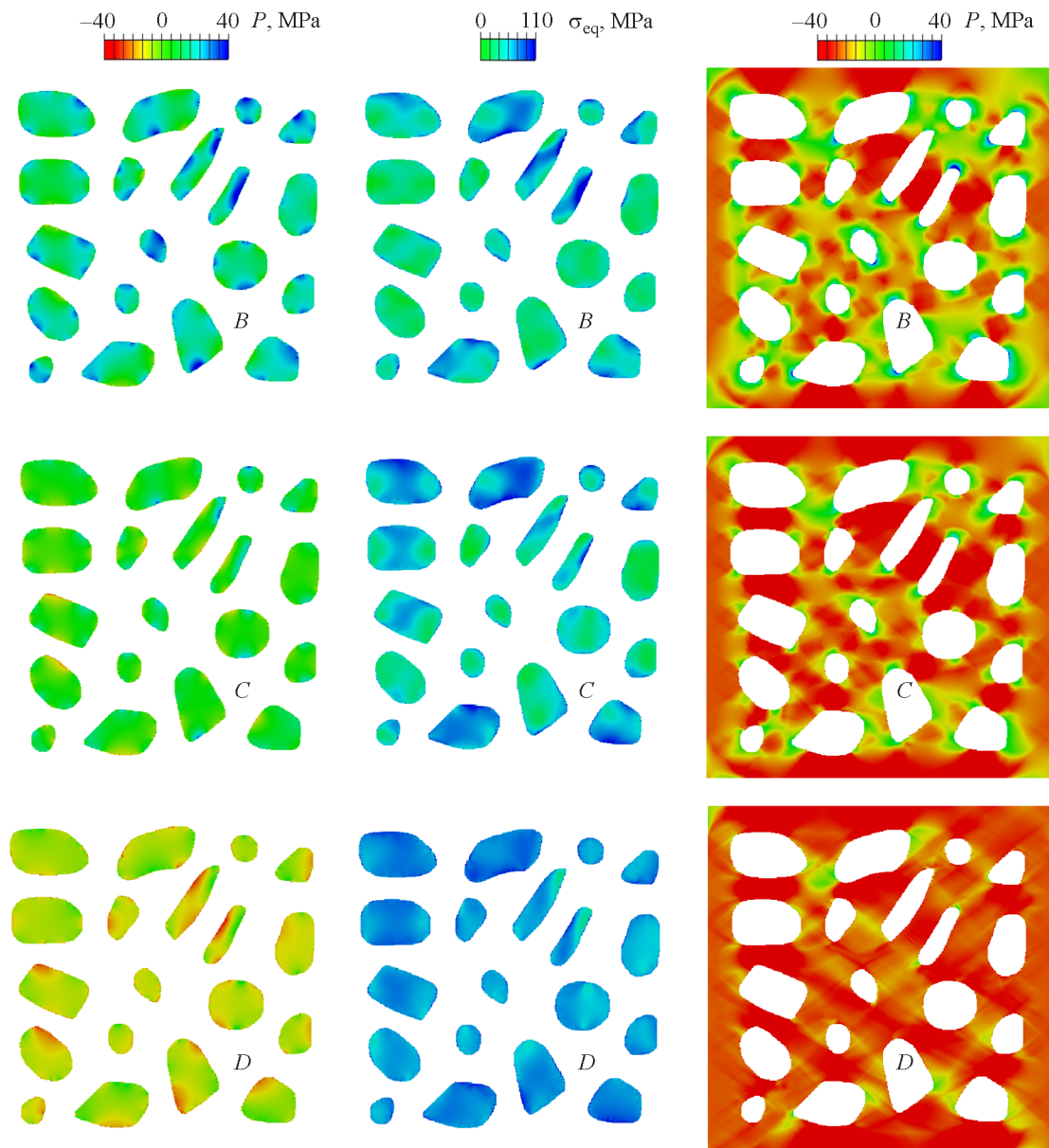


Fig. 4. Stress-strain evolution in Si particles and Al60 matrix at stages 1 and 2 under tension. States *B*, *C* and *D* (color online).

trix is negative, which confirms the conclusion that most of the matrix experiences tensile loads after cooling.

3.2. Effect of Residual Stresses and the Yield Point of the Matrix on the Strength of the Eutectic

With increasing yield point of aluminum, the average level of residual stresses after cooling of the eutectic increases (Fig. 2a). Aluminum Al60 has the highest yield point and deforms elastically during cooling for a longer time than other alloys, as evidenced by a longer linear portion in Fig. 2a, which is

due to the absence of plastic strains in the range $\varepsilon = 0.5\text{--}0.4\%$ (Fig. 2b). Then, the flow stress increases nonlinearly due to plastic shearing in the matrix around the particles.

The role of residual stresses is investigated by comparing stretching from the initial unstrained state (NRS) with stretching after cooling (RS). It is shown that at the beginning of stage 1 (up to approximately 0.5% strain of Al60-Si composite), despite the higher average stress level in the RS case than in the NRS case (Fig. 6b), residual stresses play a positive role because the particles are completely compressed (Fig. 5b) and thus “protected” from fracture. The po-

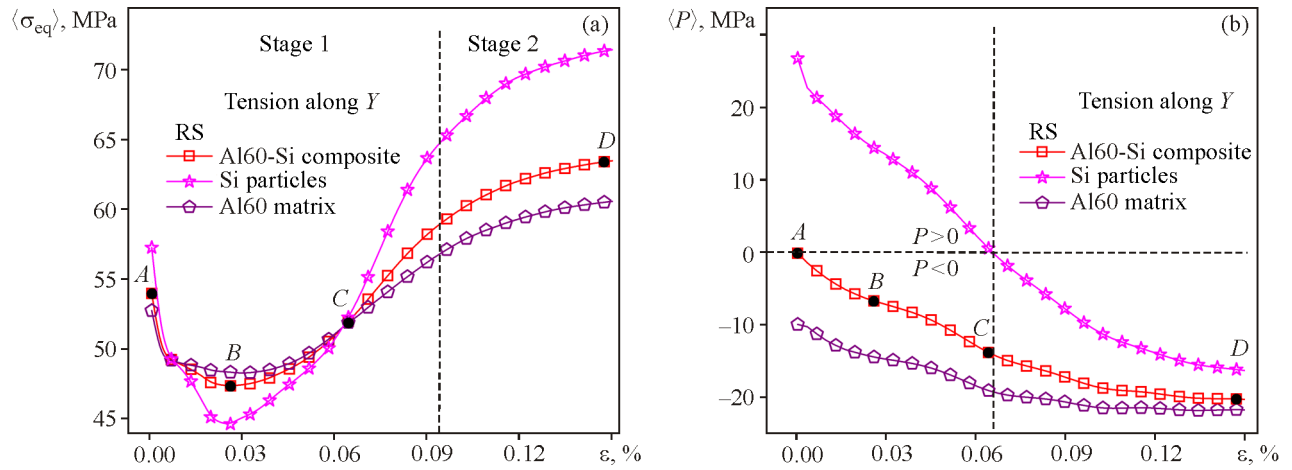


Fig. 5. Averaged equivalent stress (a) and pressure (b) in silicon particles and aluminum matrix at stages 1 and 2 of composite deformation (color online).

sitive role of residual stresses in the later part of stage 1 (from 0.5 to 1.1% strain) is due to the lower stress level in the particles in the RS case than in the NRS case (Fig. 6b), regardless of whether the pressure is positive or negative (Fig. 5b).

With further loading at stage 2, tensile stresses appear in the particles, and the average equivalent stress becomes greater in the RS case. This happens because the rate of stress increase at stages 1 and 2 in the RS case is greater than in the NRS case, which is

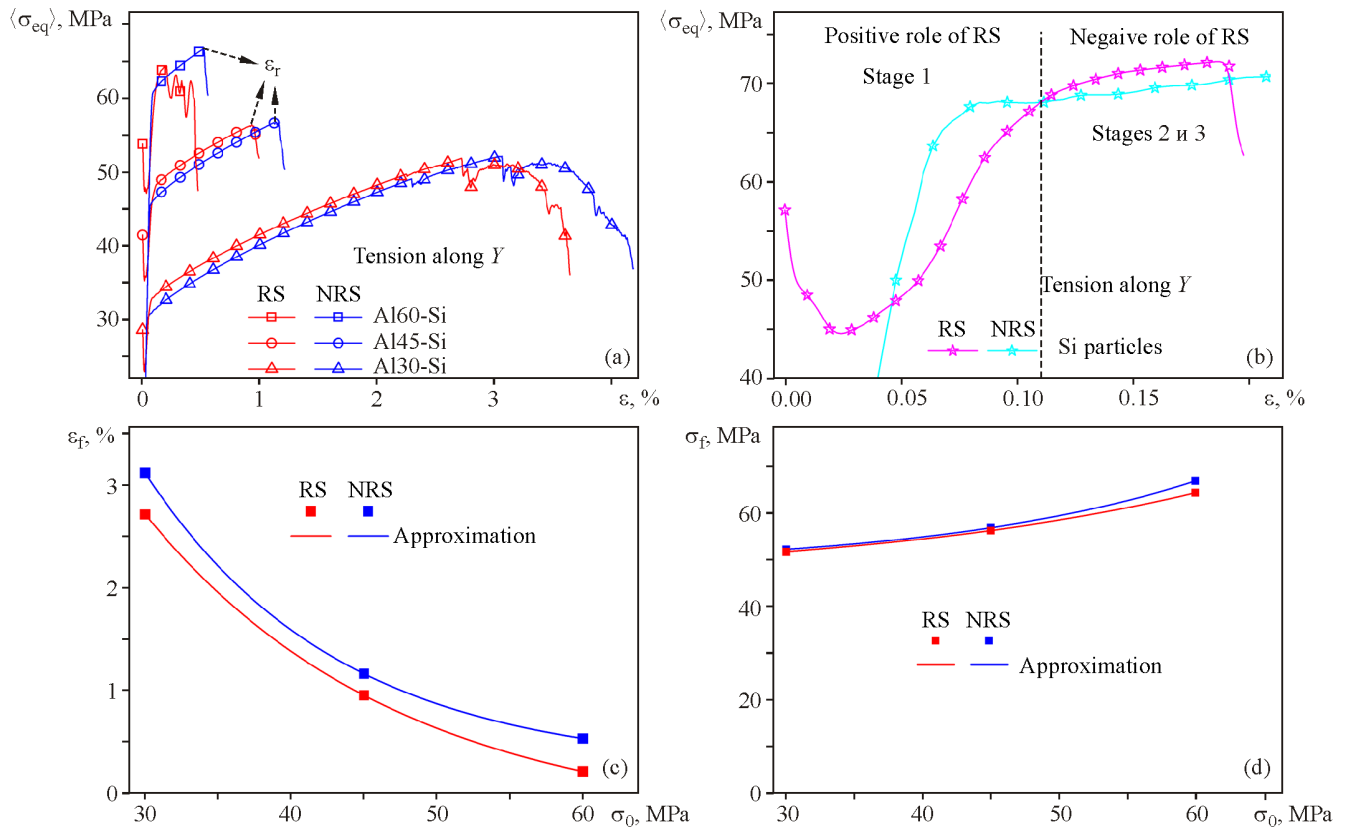


Fig. 6. Averaged flow curves of a composite with different matrix yield point (a), effect of residual stresses on the average stress level in silicon particles (b), dependence of strain ϵ_f (c) and stress σ_f (d) before the onset of eutectic fracture on the yield point of the matrix (color online).

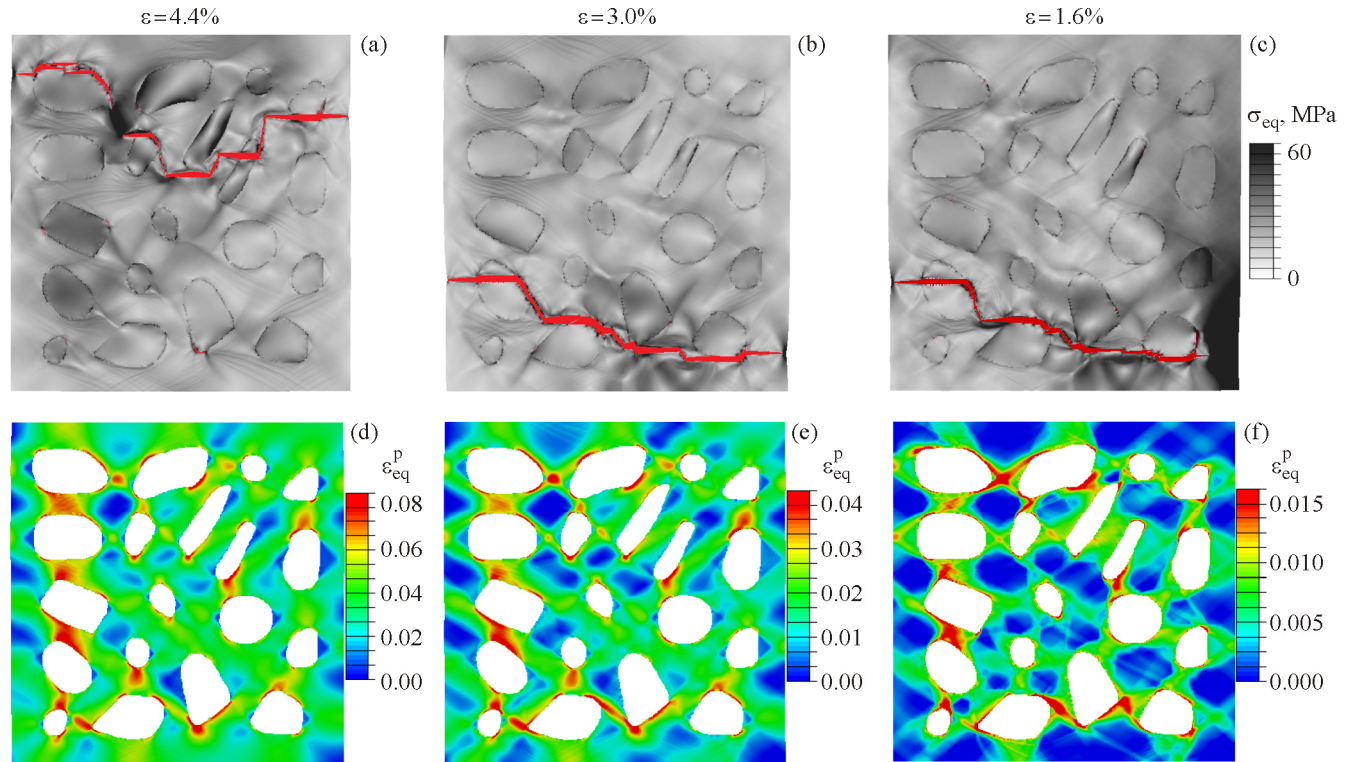


Fig. 7. Stress patterns with fracture paths under tension along Y for composites with different matrix materials Al30 (a), Al45 (b) and Al60 (c) in the RS case and the corresponding plastic strain distributions at the prefracture stage (d–f) (color online).

due to preliminary plastic deformation of aluminum at the cooling stage (cf. the slope of the cyan and pink curves in Fig. 6b). As a result, the crack initiates earlier in the RS case and the flow curve shows a descending trend, while in the NRS case the composite continues to deform elastoplastically. Thus, at later stages of eutectic deformation, residual stresses play a negative role, reducing the strength of the composite. Calculations showed that this conclusion is valid for all considered yield point values of the matrix (cf. the blue curve for the NRS case and the red curve for the RS case in Fig. 6a). The difference lies in the length of stage 2, which precedes fracture and is associated with a monotonic stress increase in the entire composite. Figure 6c shows the dependence of the composite strain ε_f (see Fig. 6a), at which fracture of the eutectic begins, on the yield point of the matrix material. It should be noted that a sharp drop in stress on the flow curves corresponds to the onset of silicon fracture, and a smooth decrease is due to crack initiation and growth in the aluminum matrix. The value of ε_f decreases exponentially with increasing matrix yield point σ_0 for both RS and NRS cases. This is because the higher σ_0 , the greater the stress concentration in local regions of particles at the elastic stage of material deformation and, accordingly, the less

stretching the composite requires in order for this concentration to reach the critical value of the silicon tensile strength of 175 MPa (Table 1). It was found that with a 2-fold increase in the yield point, the elongation to failure ε_f of the composite decreases by a factor of 6 (from 3% for Al30 to 0.5% for Al60), while the strength of the composite σ_f changes slightly by 20–25% (51 MPa for Al30 and 66 MPa for Al60). For all matrices, ε_f is greater in the NRS case than in the RS case, which is due to a higher rate of equivalent stress increase in particles under thermo-mechanical loading than under mechanical loading. At low values of the matrix yield point, the influence of residual stresses on the strength of the composite becomes minimal (Fig. 6d).

In all cases considered, cracks in the composite initiate and grow by the following mechanism. First cracks appear in brittle silicon particles. The crack tip regions at the interface with the matrix are zones of high local stress concentration, which causes rapid accumulation of plastic strains in the adjacent regions of the aluminum matrix. The strains increase rapidly to a critical value and the matrix begins to crack. The final appearance of the cracks is shown in Figs. 7a–7c. The general fracture pattern is the same for all matrix materials studied, showing a main crack ori-

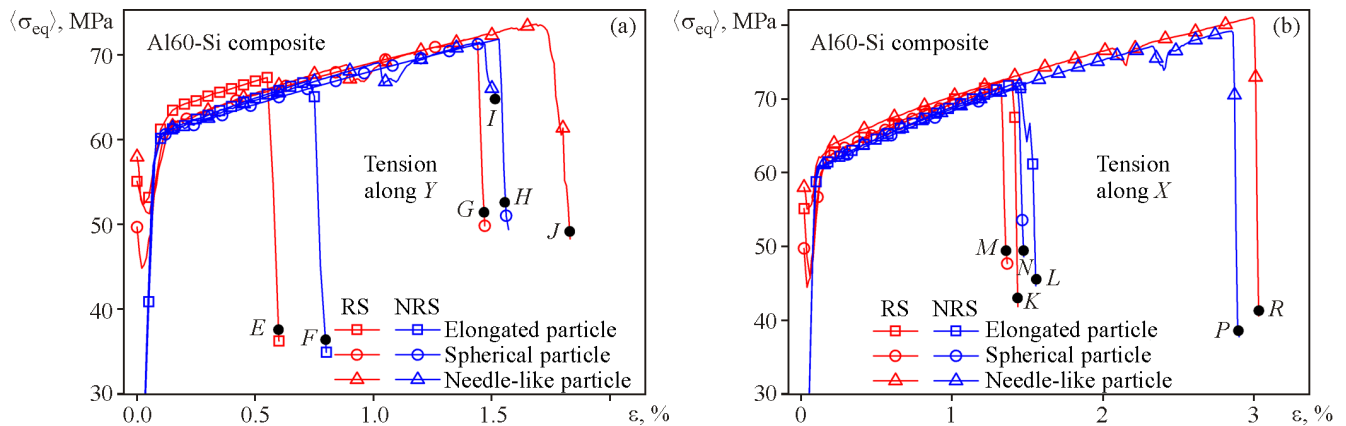


Fig. 8. Averaged flow curves of a unit volume of the eutectic with particles of different shape under tension in different directions Y (a) and X (b) with account (RS) and without account for thermally induced residual stresses (NRS) (color online).

ented predominantly perpendicular to the tensile direction. However, the location of the crack initiation site is different at low and high yield points. At low yield point of the matrix, fracture occurs later; there is sufficient time for full plastic flow to develop in the matrix (Fig. 7d). This leads to stress redistribution in the particles compared to the cases with high yield points, when the plastic flow is mostly localized around the particles and the matrix regions surrounded by the particles are slightly deformed or are in the elastic state (Figs. 7e and 7f).

3.3. Effect of Silicon Particle Morphology on the Fracture Behavior and Strength of the Eutectic

Experiments showed that silicon particles in the eutectic have different shapes and orientations with respect to the applied load direction (Fig. 1b). Let us analyze the influence of the morphology of a single silicon particle on the behavior of a unit volume of the eutectic. Numerical calculations were carried out for a composite with an elongated (Fig. 1d, particle 1), needle-like (Fig. 1d, particle 2) and spherical particle (Fig. 1d, particle 3). The matrix material was aluminum with a yield point of 60 MPa. It was found that the composite with a needle-like silicon particle had the greatest strength under tension along X after cooling (Fig. 8b, red curve with triangles). Depending on the stretching direction, the lowest strength was observed for either an elongated particle (under tension along Y) or a particle with a perfect spherical shape (under tension along X).

The increase in the total strain to failure of the composite with decreasing curvature of the matrix–particle interface is associated with the absence of local stress concentration at heterogeneities. For a

needle-like particle, the eutectic strength increases because the particle is oriented at an angle of 45° to the applied load direction, i.e., in the direction of maximum tangential stresses. It was also found for such particles that residual stresses arising after cooling of the eutectic enhance the tensile strength of the composite in both directions (cf. the red and blue curves with triangular symbols in Figs. 8a and 8b). For spherical and ellipsoidal particles oriented in the applied load directions, residual stresses play a negative role (cf. the red and blue curves with round and square symbols in Figs. 8a and 8b).

Analysis of the stress-strain and fracture behavior revealed the following. The closer the particle shape is to spherical, the more likely fracture will occur along the interface (Fig. 9, states G , M , H , N). Elongated particles, whose axes are oriented parallel or perpendicular to the applied load direction, tend to split (Fig. 9, states E , K , F , L). When elongated particles are oriented in the direction of maximum shear stresses, a mixed fracture mode is observed (Fig. 9, states J , R , I , P).

4. CONCLUSIONS

Experimental and numerical studies were performed on AlSi12 alloy produced by wire-feed electron beam additive manufacturing to examine the structure and the effect of cooling-induced residual stresses on the mechanical properties of a eutectic microvolume. Dynamic boundary value problems were solved in a two-dimensional formulation using the ABAQUS/Explicit finite element code. The thermomechanical response of the materials was described using the Duhamel–Neumann relations. The simulations were performed by taking into account the

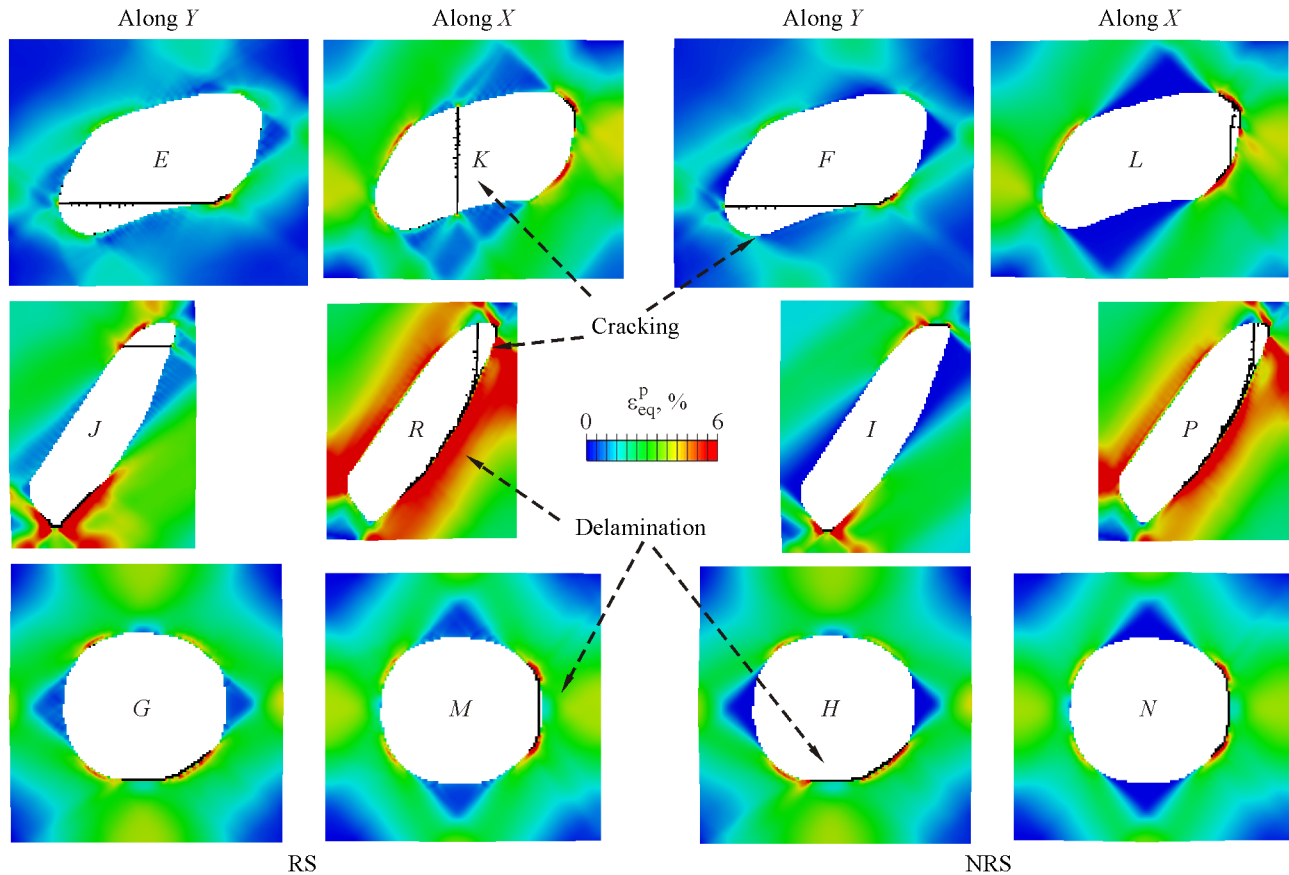


Fig. 9. Plastic strain distributions in the Al60 matrix and fracture patterns in Si particles of various shapes during tension of the composite. States *E–R* are marked in Fig. 8 (color online).

fracture of both silicon particles and the aluminum matrix. The influence of the matrix yield point and particle morphology on the strength of the composite was studied. The simulation results led to the following conclusions.

Cooling the eutectic from a temperature of 350 to 23°C causes residual stresses and plastic strains due to the difference in the thermoelastic properties of aluminum and silicon. The particles experience bulk compression, and the matrix is under both compression and tension. The flow curves of the eutectic under tension can be divided into stages. The first stage is associated with the change of the multiaxial stress state induced by cooling of the composite to a uniaxial stress state. The stress drop on the flow curve corresponds to the transition of silicon particles from a compressed state to a stretched state. The second stage is characterized by a monotonic increase in the stress concentration in the particles and plastic strain localization in the matrix. The third stage corresponds to fracture of the eutectic.

The relative elongation to failure of the eutectic phase increases exponentially with decreasing aluminum yield point, and the ultimate fracture stress changes slightly. It was shown that cooling-induced residual stresses negatively affect the strength of the eutectic for all considered values of the matrix yield point. This is because the rate of increase in tensile stress concentration in particles is greater under thermomechanical loading than under mechanical loading.

The orientation of elongated particles in the direction of maximum tangential stresses has the most positive effect on the strength of the eutectic. With the given particle morphology, residual stresses enhance the strength of the composite. The closer the particle shape is to spherical, the more likely fracture will occur along the matrix–particle interface.

FUNDING

The study was supported by Russian Science Foundation Grant No. 23-11-00222, <https://rscf.ru/en/project/23-11-00222/>

CONFLICT OF INTEREST

The authors of this work declare that they have no conflicts of interest.

OPEN ACCESS

This article is licensed under a Creative Commons Attribution 4.0 International License, which permits use, sharing, adaptation, distribution and reproduction in any medium or format, as long as you give appropriate credit to the original author(s) and the source, provide a link to the Creative Commons license, and indicate if changes were made. The images or other third party material in this article are included in the article's Creative Commons license, unless indicated otherwise in a credit line to the material. If material is not included in the article's Creative Commons license and your intended use is not permitted by statutory regulation or exceeds the permitted use, you will need to obtain permission directly from the copyright holder. To view a copy of this license, visit <http://creativecommons.org/licenses/by/4.0/>

REFERENCES

- Zolotarevsky, V.S., Belov, N.A., and Glazoff, M.V., *Casting Aluminum Alloys*, Amsterdam: Elsevier Ltd., 2007.
- Apelian, D., *Aluminum Cast Alloys: Enabling Tools for Improved Performance*, Wheeling, USA: NADCA, 2009.
- Ye, H., An Overview of the Development of Al-Si Alloy Based Material for Engine Applications, *J. Mater. Eng. Perform.*, 2003, vol. 12, pp. 288–297.
- Zamani, M., *Microstructure and Mechanical Properties at Ambient and Elevated Temperature Al-Si Cast Alloys*, Jönköping, Sweden: School of Engineering, Jönköping University, 2015. <http://hj.diva-portal.org/smash/get/diva2:814885/FULLTEXT01.pdf>
- Makhlouf, M.M. and Guthy, H.V., The Aluminum-Silicon Eutectic Reaction: Mechanisms and Crystallography, *J. Light Met.*, 2001, vol. 1, pp. 199–218. [https://doi.org/10.1016/S1471-5317\(02\)00003-2](https://doi.org/10.1016/S1471-5317(02)00003-2)
- Shankar, S., Riddle, Y.W., and Makhlouf, M.M., Nucleation Mechanism of the Eutectic Phases in Aluminum-Silicon Hypoeutectic Alloys, *Acta Mater.*, 2004, vol. 52, pp. 4447–4460. <https://doi.org/10.1016/j.actamat.2004.05.045>
- Yang, Y., Chen, Y., Zhang, J., Gu, X., Qin, P., Dai, N., Li, X., Kruth, J.-P., and Zhang, L., Improved Corrosion Behavior of Ultrafine-Grained Eutectic Al-12Si Alloy Produced by Selective Laser Melting, *Mater. Design*, 2018, vol. 146, pp. 239–248. <https://doi.org/10.1016/j.matdes.2018.03.025>
- Farshidianfar, M.H., Khajepour, A., and Gerlich, A.P., Effect of Real-Time Cooling Rate on Microstructure in Laser Additive Manufacturing, *J. Mater. Process. Technol.*, 2016, vol. 231, pp. 468–478. <https://doi.org/10.1016/j.jmatprotec.2016.01.017>
- Thampy, V., Fong, A.Y., Calta, N.P., Wang, J., Martin, A.A., Depond, P.J., Kiss, A.M., Guss, G., Xing, Q., Ott, R.T., van Buuren, A., Toney, M.F., Weker, J.N., Kramer, M.J., Matthews, M.J., Tassone, C.J., and Stone, K.H., Subsurface Cooling Rates and Microstructural Response During Laser Based Metal Additive Manufacturing, *Sci. Rep.*, 2020, vol. 10, pp. 1–9. <https://doi.org/10.1038/s41598-020-58598-z>
- Chou, R., Milligan, J., Paliwal, M., and Brochu, M., Additive Manufacturing of Al-12Si Alloy Via Pulsed Selective Laser Melting, *JOM*, 2015, vol. 67, pp. 590–596. <https://doi.org/10.1007/s11837-014-1272-9>
- Olakanmi, E.O., Cochrane, R.F., and Dalgarno, K.W., Densification Mechanism and Microstructural Evolution in Selective Laser Sintering of Al-12Si Powders, *J. Mater. Process. Technol.*, 2011, vol. 211, pp. 113–121. <https://doi.org/10.1016/j.jmatprotec.2010.09.003>
- Siddique, S., Wycisk, E., Frieling, G., Emmelman, C., and Walter, F., Microstructural and Mechanical Properties of Selective Laser Melted Al 4047, *Appl. Mech. Mater.*, 2015, vol. 752–753, pp. 485–490. <https://doi.org/10.4028/www.scientific.net/AMM.752-753.485>
- Gokuldoss Prashanth, K., Scudino, S., and Eckert, J., Tensile Properties of Al-12Si Fabricated Via Selective Laser Melting (SLM) at Different Temperatures, *Technologies*, 2016, vol. 4, p. 38. <https://doi.org/10.3390/technologies4040038>
- Da Silva, A., Wang, S., Volpp, J., and Kaplan, A.F.H., Vertical Laser Metal Wire Deposition of Al-Si Alloys, *Proc. CIRP*, 2020, vol. 94, pp. 341–345. <https://doi.org/10.1016/j.procir.2020.09.078>
- Huang, W., Chen, S., Xiao, J., Jiang, X., and Jia, Y., Laser Wire-Feed Metal Additive Manufacturing of the Al Alloy, *Optics Laser Technol.*, 2021, vol. 134, p. 106627. <https://doi.org/10.1016/j.optlastec.2020.106627>
- Utyaganova, V., Filippov, A., Tarasov, S., Shamarin, N., Gurianov, D., Vorontsov, A., Chumaevskii, A., Fortuna, S., Savchenko, N., Rubtsov, V., and Kolu-baev, E., Characterization of AA7075/AA5356 Gradient Transition Zone in an Electron Beam Wire-Feed Additive Manufactured Sample, *Mater. Character.*, 2021, vol. 172, p. 110867. <https://doi.org/10.1016/j.matchar.2020.110867>
- Balokhonov, R.R., Romanova, V.A., Schmauder, S., and Emelianova, E.S., A Numerical Study of Plastic Strain Localization and Fracture Across Multiple Spatial Scales in Materials with Metal-Matrix Composite Coatings, *Theor. Appl. Fract. Mech.*, 2019, vol. 101, pp. 342–355. <https://doi.org/10.1016/j.tafmec.2019.03.013>
- Balokhonov, R.R., Romanova, V.A., Buyakova, S.P., Kulkov, A.S., Bakeev, R.A., Evtushenko, E.P., and

- Zemlyanov, A.V., Deformation and Fracture Behavior of Particle-Reinforced Metal Matrix Composites and Coatings, *Phys. Mesomech.*, 2022, vol. 25, no. 6, pp. 492–504. <https://doi.org/10.1134/S1029959922060029>
19. Balokhonov, R.R., Kulkov, A.S., Zemlyanov, A.V., Romanova, V.A., Evtushenko, E.P., Gatiyatullina, D.D., and Kulkov, S.N., Evolution of Residual Stresses and Fracture in Thermomechanically Loaded Particle-Reinforced Metal Matrix Composites, *Phys. Mesomech.*, 2021, vol. 24, no. 5, pp. 503–512. <https://doi.org/10.1134/S1029959921050015>
 20. Balokhonov, R., Romanova, V., Schwab, E., Zemliyanov, A., and Evtushenko, E., Computational Microstructure-Based Analysis of Residual Stress Evolution in Metal-Matrix Composite Materials during Thermo-mechanical Loading, *Facta Univ. Mech. Eng.*, 2021, vol. 19, no. 2, pp. 241–252. <https://doi.org/10.22190/FUME201228011B>
 21. Ma, P., Jia, Y., Prashanth, K.G., Yu, Zh., Li, Ch., Zhao, J., Yang, S., and Huang, L., Effect of Si Content on the Microstructure and Properties of Al-Si Alloys Fabricated Using Hot Extrusion, *J. Mater. Res.*, 2017, vol. 32, pp. 2210–2217. <https://doi.org/10.1557/jmr.2017.97>
 22. Wejrzanowski, T., Lewandowska, M., and Kurzydłowski, K.J., Stereology of Nano-Materials, *Image Analys. Stereol.*, 2011, no. 1(29), pp. 1–12. <https://doi.org/10.5566/ias.v29.p1-12>